

Arginylation of β -Actin Regulates Actin Cytoskeleton and Cell Motility

Marina Karakozova,¹ Marina Kozak,¹ Catherine C. L. Wong,² Aaron O. Bailey,² John R. Yates III,² Alexander Mogilner,³ Henry Zebroski,⁴ Anna Kashina^{1*}

Posttranslational arginylation is critical for mouse embryogenesis, cardiovascular development, and angiogenesis, but its molecular effects and the identity of proteins arginylated *in vivo* are unknown. We found that β -actin was arginylated *in vivo* to regulate actin filament properties, β -actin localization, and lamella formation in motile cells. Arginylation of β -actin apparently represents a critical step in the actin N-terminal processing needed for actin functioning *in vivo*. Thus, posttranslational arginylation of a single protein target can regulate its intracellular function, inducing global changes on the cellular level, and may contribute to cardiovascular development and angiogenesis.

Protein arginylation is an enigmatic post-translational modification discovered more than 40 years ago (1) and poorly understood on the molecular level. Arginylation is mediated by Arg-transfer RNA (-tRNA) protein transferase (Ate1) (2, 3), which transfers arginyl from tRNA onto the N terminus of proteins, forming a peptide bond. Three N-terminal residues, Asp, Glu, and Cys, can be arginylated, requiring prior posttranslational modification by Met-aminopeptidation or proteolysis.

Ate1 is an evolutionarily conserved enzyme that is essential for embryonic development. Ate1 knockout in mice results in embryonic lethality and severe defects in cardiovascular development and angiogenesis (4). Thus, arginylation is important for the regulation of the physiological functions of key proteins *in vivo*. However, its molecular effects and the identity of arginylated proteins are unknown.

We examined the role of protein arginylation in the regulation of a single protein target with effects on the molecular and cellular level.

β -actin is arginylated *in vivo*. Actin undergoes N-terminal processing *in vivo* by acetylation and removal of the first Met residue, followed by acetylation, and in some cases, removal of the second residue (5–10). This processing would result in N-terminal exposure of an arginylatable residue in all actin isoforms: Asp2 or Asp3 in β -actin, Glu2 or Glu3 in γ -actin, and Cys2 or Asp3 in α -actin, suggesting that actin could become a target for arginylation *in vivo*.

To find whether any of the actin isoforms could be arginylated *in vivo*, we fractionated whole lysates from mouse embryonic fibroblasts by two-dimensional (2D) gel electrophoresis, excised the spot corresponding to actin, and analyzed it by in-gel digestion followed by

mass spectrometry (MS) (Fig. 1). This preparation predominantly contained a mixture of β and γ -actin with a small amount of α -actin, which is consistent with the actin isoform composition reported for embryonic fibroblasts (11). Both β and γ -actin were identified with >80% sequence coverage. We found peptides ending with N-terminal Met1, Glu2, and Glu3 of the γ -actin sequence, indicating that γ -actin had undergone sequential N-terminal removal of both first and second residues. However, we were unable to find any peptides corresponding to the N terminus of β -actin, suggesting that the β -actin N terminus was either undetectable by MS or had undergone additional N-terminal processing.

To test the hypothesis that actin had undergone arginylation, we introduced new sequences into the sequence database, adding Arg sequentially onto every arginylatable amino acid residue in the actin sequence for each identified isoform (Asp, Glu, Cys, and Asn deamidated to Asp, and Gln deamidated to Glu). We then repeated the search using the resulting database. This search yielded a new peptide, where an Arg residue was found on the N terminus of Asp3 of the β -actin sequence (Fig. 1A).

To confirm that the newly identified peptide was indeed arginylated, we compared its mass and tandem mass spectrum to the synthetic peptides corresponding to residues 1 to 17 of the actin N-terminal sequence (similar to the peptide yielded by cleavage with endopeptidase LysC), modified by the removal of Met1 and acetylation of Asp2 or the removal of Met1 and Asp 2 and arginylation of Asp3. Both peptides were found in actin preparations, confirming that both acetylated and arginylated forms of actin are found *in vivo*.

To make an estimate of what percentage of the intracellular actin was arginylated, we performed immunoprecipitation of actin from the lysates of wild-type mouse embryonic fibroblasts and fibroblasts from the knockout mice deficient in arginylation enzyme Ate1 [Ate1^{-/-} mice (4)] and fractionated the resulting actin precipitates on 2D gels under conditions that

allowed the separation of different actin isoforms (pH range 4 to 8). The addition of Arg onto β -actin would be expected to shift its isoelectric point (pI) into the more basic range without changing its molecular weight. Although in Ate1^{-/-} cell extracts the majority of actin was found in two spots (spots 1 and 2 in Fig. 1C, consistent with the unmodified β and γ -actin isoforms and containing β and γ N-terminal peptides, respectively), in the wild-type extracts there was a redistribution of protein toward the more basic pI range, resulting in the enlargement of the more basic (γ -actin) spot, reduction of the more acidic (β -actin) spot, and the appearance of an additional relatively major basic spot (spot 3 in Fig. 1C). The more basic spots 2 and 3 in the wild-type cells contained arginylated β -actin peptide, as confirmed by MS. The total shift of actin into the basic pI range in wild-type cells is likely to reflect the amount of actin arginylated *in vivo*, and corresponded to approximately 20% of total actin, which corresponds to approximately 40% of intracellular β -actin. Thus, we find that β -actin is arginylated *in vivo*.

Arginylation prevents actin filaments from clustering. To study which property of actin is affected by arginylation, we tested metabolic stability, the composition of actin-binding proteins, and polymerization properties of actin in the absence and presence of arginylation.

It has been suggested that N-terminal arginylation marks proteins for ubiquitin-dependent degradation by the N-end rule pathway (12). To check whether arginylation affects the metabolic stability of actin, we performed a cycloheximide chase of total actin and a pulse chase of β -actin in wild-type and Ate1^{-/-} cells (Fig. 2A). In both cell types, total actin and β -actin remained stable over a time course of 6 hours, with no apparent changes in the kinetics or protein level in wild-type as compared to Ate1^{-/-} cells. Moreover, we found no changes in the stationary level of β -actin in wild-type as compared to Ate1^{-/-} cells, indicating that actin stability over longer times was probably not affected by arginylation. Thus, arginylation does not induce β -actin degradation.

To determine whether arginylation affects the ability of β -actin to bind other intracellular proteins, we performed immunoprecipitations of actin from wild-type and Ate1^{-/-} cell extracts and analyzed the resulting preparations by MS. We found no major changes in the protein composition of the immunoprecipitates in either cell type.

To determine whether arginylation affects the ability of actin to form filaments, we performed polymerization assays in wild-type and Ate1^{-/-} cell extracts, using a pyrenyl-actin assay (13, 14) (Fig. 2B). Although the initial polymerization rate and kinetics were similar in both types of extracts, pyrenyl fluorescence in Ate1^{-/-} extracts exhibited a sharp drop after the initial rapid increase, suggesting that actin filaments in

¹Department of Animal Biology, University of Pennsylvania, Philadelphia, PA 19104, USA. ²The Scripps Research Institute, La Jolla, CA 92037, USA. ³University of California, Davis, CA 95616, USA. ⁴The Rockefeller University, New York, NY 10021, USA.

*To whom correspondence should be addressed. E-mail: akashina@vet.upenn.edu

Ate1^{-/-} extracts underwent aggregation. Similar results were obtained if actin polymerization in extracts was induced by the addition of seeds or of recombinant activator of the actin nucleator complex Arp2/3.

Because the addition of exogenous pyrenyl actin introduced wild-type actin protein into the extracts, it may have affected polymerization of the endogenous actin. To exclude this possibility, we performed spontaneous polymerization experiments in the cell extracts in the absence of exogenously added factors and then visualized the polymerized filaments by rhodamine-phalloidin staining followed by fluorescence microscopy (Fig. 2C). Actin filaments in the control extracts formed single filaments, whereas in

Ate1^{-/-} extracts the filaments appeared clustered, forming random filamentous aggregates (Fig. 2C).

To confirm that the observed filament clustering is the property of actin itself and not of other factors found in the extract, we incubated rhodamine-phalloidin-labeled filaments, pre-polymerized from purified rabbit skeletal muscle actin, in the *Ate1*^{-/-} extracts. Such pre-polymerized filaments did not cluster or aggregate in *Ate1*^{-/-} extracts (Fig. 2C), suggesting that the clustering was the property of the arginylation-free actin filaments and not of additional factors in the *Ate1*^{-/-} extracts. Thus, the absence of protein arginylation causes actin to form aggregates in cell extracts by changing the properties of the nonargylylated actin filaments.

Arginylation regulates cell motility. To study the effect of arginylation on the intracellular functions of β -actin, we compared the morphology, motility, and actin cytoskeleton of wild-type and *Ate1*^{-/-} cells. The majority of *Ate1*^{-/-} cells appeared smaller than wild-type cells and were apparently unable to form a lamella during movement along the substrate (Fig. 3). Time-lapse imaging of single cells (Fig. 3A and videos S1 and S2) or of a fibroblast monolayer moving into the wound (Fig. 3C and videos S3 and S4) confirmed that although both types of cells were apparently motile, *Ate1*^{-/-} cells failed to form normal lamellae during motility, resulting in their inability to cover the same distance or occupy the same area of the substrate as the control cells. In addition,

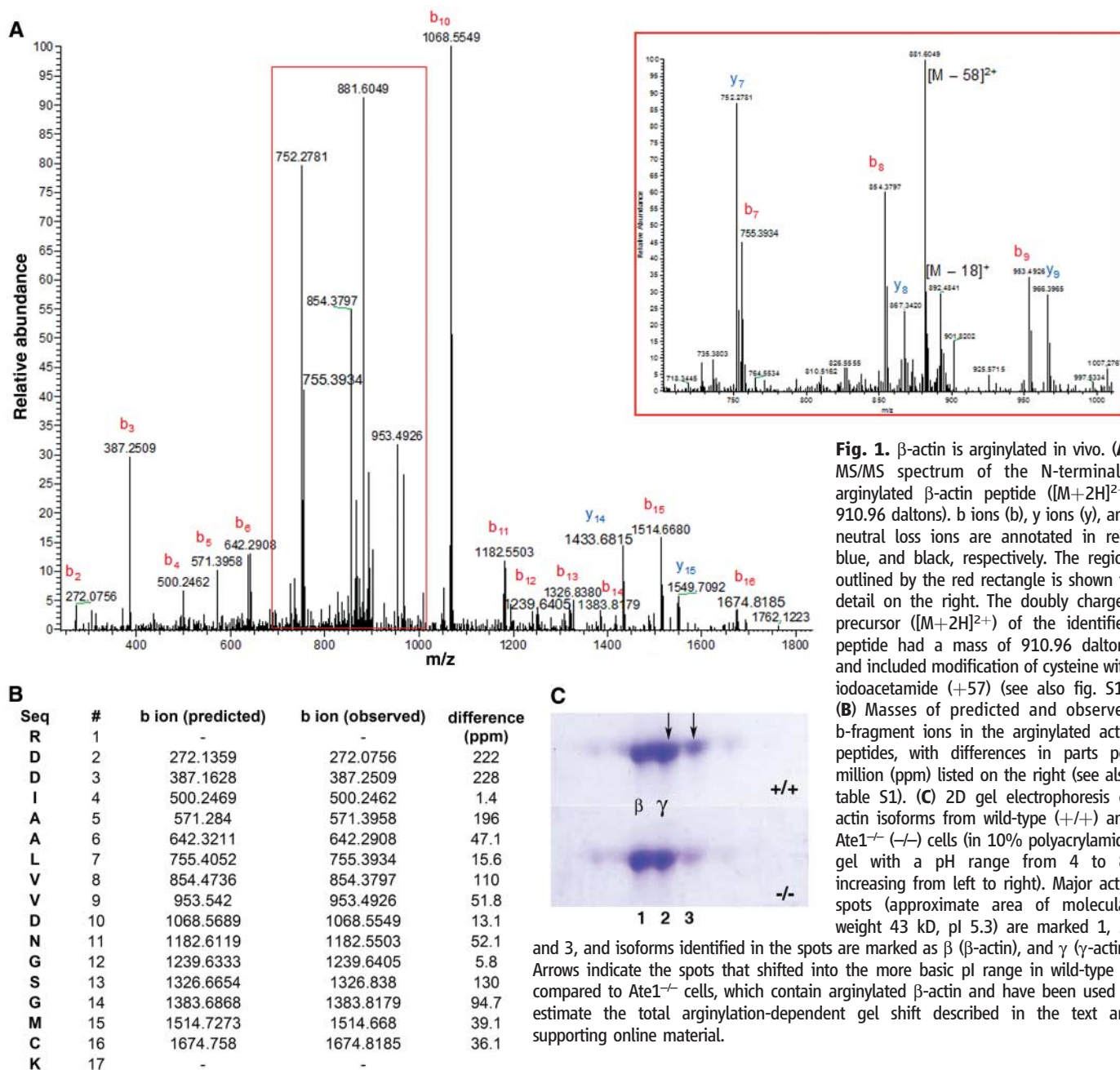


Fig. 1. β -actin is arginylated in vivo. (A) MS/MS spectrum of the N-terminally argylylated β -actin peptide ($[M+2H]^{2+}$, 910.96 daltons). b ions (b), y ions (y), and neutral loss ions are annotated in red, blue, and black, respectively. The region outlined by the red rectangle is shown in detail on the right. The doubly charged precursor ($[M+2H]^{2+}$) of the identified peptide had a mass of 910.96 daltons and included modification of cysteine with iodoacetamide (+57) (see also fig. S1).

(B) Masses of predicted and observed b-fragment ions in the argylylated actin peptides, with differences in parts per million (ppm) listed on the right (see also table S1). (C) 2D gel electrophoresis of actin isoforms from wild-type (+/+) and *Ate1*^{-/-} (-/-) cells (in 10% polyacrylamide gel with a pH range from 4 to 8, increasing from left to right). Major actin spots (approximate area of molecular weight 43 kD, pI 5.3) are marked 1, 2,

Ate1^{-/-} cells exhibited apparent defects in ruffling activity and cortical flow (videos S1 and S2).

To confirm that the apparently smaller size of the *Ate1*^{-/-} cells was indeed due to the decreased

spreading and not to a smaller volume, we compared the ratios of cell volume and area occupied by fully spread cells in wild-type and *Ate1*^{-/-} fibroblasts (Fig. 3B). Although the volume ratio

of the two cell types was approximately 1:1 [ratio of (+/+):(-/-) = 1: 1.06, *n* = 100 cells], the average area occupied by wild-type cells was more than 2 times larger [ratio of (+/+):(-/-) =

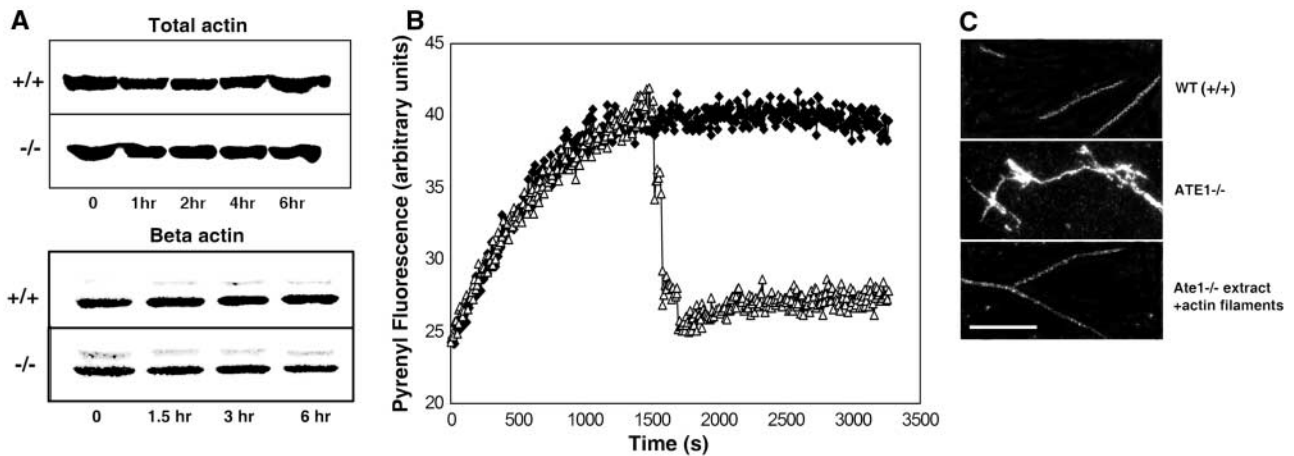
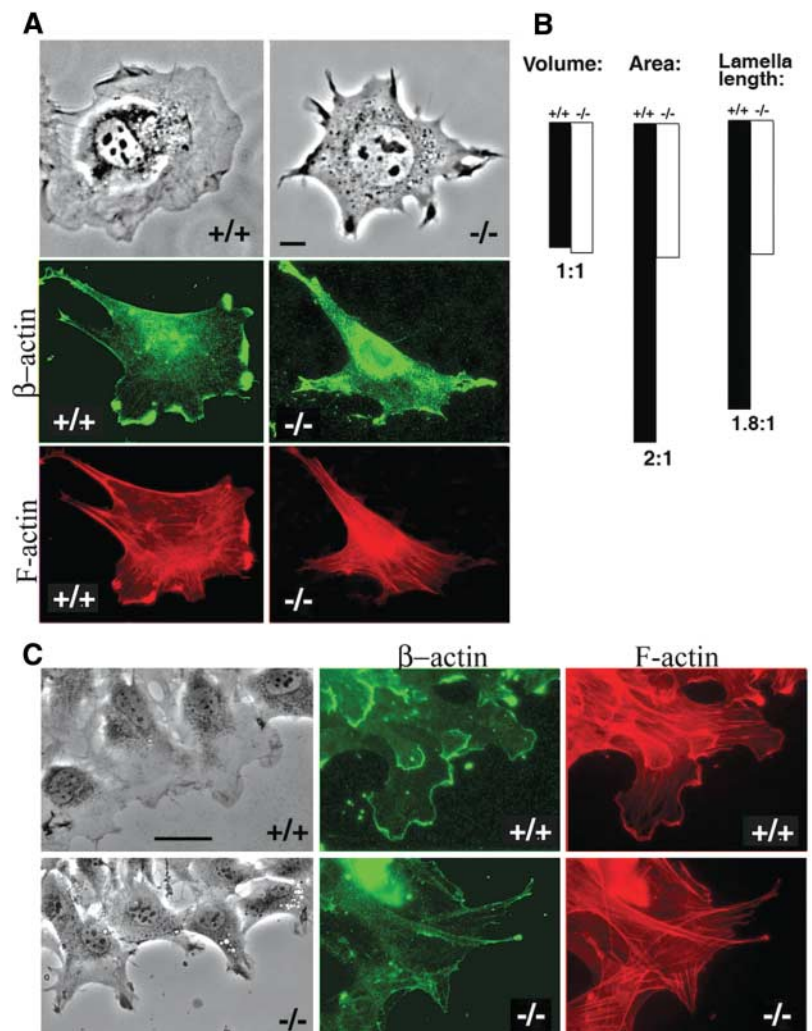


Fig. 2. Arginylation causes actin filament aggregation without affecting actin metabolic stability. **(A)** Cycloheximide chase of total actin (top) and pulse chase of β -actin (bottom) over a time course of 6 hours in wild-type (+/+) and *Ate1*^{-/-} cells. **(B)** Polymerization curves in wild-type and *Ate1*^{-/-} cell extracts measured by pyrenyl fluorescence of exogenous pyrenyl actin added to the

extracts. Solid and open symbols indicate pyrenyl fluorescence in wild-type and *Ate1*^{-/-} extracts, respectively. **(C)** Rhodamine-phalloidin-stained actin filaments spontaneously polymerized in wild-type (top) or *Ate1*^{-/-} (middle) cell extracts or pre-polymerized from exogenous actin and added to the *Ate1*^{-/-} extracts (bottom). Scale bar, 10 μ m.

Fig. 3. Arginylation regulates cell spreading, lamella formation, and intracellular localization of β -actin. **(A)** Images of single cells in wild-type (+/+, left) and *Ate1*^{-/-} (-/-, right) mouse fibroblast cultures visualized by phase contrast (top pair) or immunofluorescence staining for β -actin (middle pair) and rhodamine-phalloidin stain and rhodamine-phalloidin staining for filamentous actin (bottom pair). Scale bar, 10 μ m. See also videos S1 and S2 for time-lapse images of cells shown in the phase-contrast photographs on top. **(B)** Quantification of cell volume, cell area, and lamella length in wild-type and *Ate1*^{-/-} cells. **(C)** Images of monolayers of wild-type (+/+, top) and *Ate1*^{-/-} (-/-, bottom) cells moving into a wound, visualized by phase contrast (left pair) or immunofluorescence staining for β -actin (middle pair) and rhodamine-phalloidin staining for filamentous actin (right pair). Scale bar, 10 μ m. See also videos S3 and S4 for time-lapse images of cells shown in the phase-contrast photographs on the left.



2.13:1, $n = 75$], and the average lamella length was almost 2 times larger [ratio of (+/+):(-/-) = 1.81:1, $n = 55$], confirming that *Ate1*^{-/-} cells indeed exhibit defects in spreading and lamella formation.

We next compared the intracellular distribution of F-actin and β -actin in both cell types. Although the general appearance and distribution of F-actin were largely similar, β -actin in

Ate1^{-/-} cells formed patches and aggregates in the cytoplasm (Fig. 3A) and failed to localize to the leading edge of the fibroblasts moving into the wound (Fig. 3C), which is consistent with the in vitro evidence of actin aggregation in *Ate1*^{-/-} cells.

Thus, the absence of actin arginylation causes defects in lamella formation and intracellular distribution of β -actin. To confirm that

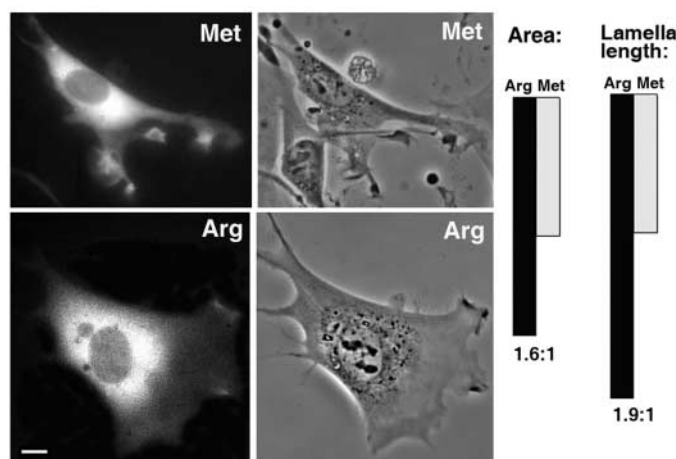
the lamella defects in *Ate1*^{-/-} cells were indeed due to the absence of β -actin arginylation, we performed a “phenotype rescue” study by transiently transfecting *Ate1*^{-/-} cells with a permanently arginylated β -actin construct, produced by a ubiquitin fusion technique (12), by replacing the Met1 and Asp2 of β -actin with Arg, followed by C-terminal fusion of the β -actin to green fluorescent protein (Arg-actin) (Fig. 4). Transfection with control constructs containing wild-type β -actin (Met-actin) caused no change in the morphology or motility of *Ate1*^{-/-} cells, but transfection with permanently arginylated β -actin resulted in the cells forming normal lamellae [ratio of Arg:Met = 1.9:1, $n = 46$; compared to a 1.81:1 ratio of (+/+):(-/-)], without fully restoring the area on the substrate [ratio of Arg:Met = 1.52:1, $n = 55$, compared to a 2.1:1 ratio of (+/+):(-/-)], ruffling activity, or cortical flow, suggesting that other arginylated proteins may be responsible for additional phenotypes in *Ate1*^{-/-} cells. Thus, arginylation of β -actin controls actin polymerization and lamella formation in motile cells.

Discussion. We found that protein arginylation can produce global effects on the molecular and cellular levels by regulating a single protein target. Arginylation apparently constitutes a next step in actin N-terminal processing, shown to be important for actin function in vivo (9, 10). Indeed, the absence of N-terminal Arg caused severe effects on actin polymerization and induced filament aggregation in vitro and β -actin redistribution in vivo.

Based on the known crystal structure of the actin molecule and the information about the intracellular architecture of actin filaments, we propose a model of how arginylation regulates actin function at the leading edge (Fig. 5). Crystal structures of the actin monomers and oligomers suggest that the actin N terminus is exposed on the surface of the actin monomers (Fig. 5A) and actin filaments upon polymerization (15). In the absence of Arg, actin filaments are mildly negatively charged because of the presence of Asp/Glu side chains and N-terminal acetyl groups. The addition of Arg introduces a bulky positively charged group onto the filament surface. Assuming that each fifth subunit of actin is arginylated (corresponding to the 20% estimation found in our experiments), the assembly of actin filaments from such a mixture should produce filaments evenly coated with bulky positive charges (approximately one per half-turn of the helix of the actin filament; see the calculation in the supporting online material) (Fig. 5B). It is conceivable that such a coating would prevent arginylated filaments from coming together into bundles and aggregates, whereas the absence of such a coating would cause filaments to aggregate, producing the effects seen in vitro.

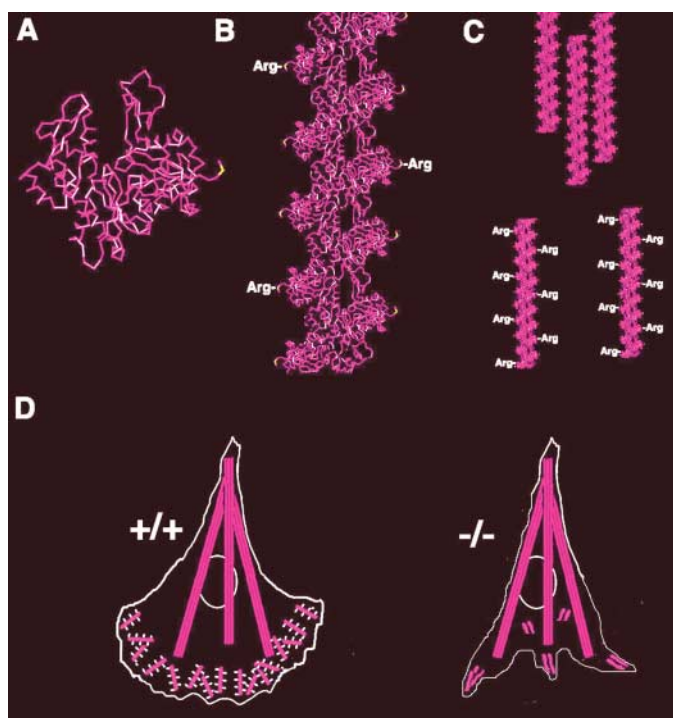
In vivo, the situation is more complex. β -actin mRNA localizes to the cell leading edge, where β -actin is rapidly produced to facilitate lamellar activity (16). β - and γ -actin in vivo are

Fig. 4. Permanently arginylated β -actin restores lamella formation in *Ate1*^{-/-} cells. **(Left)** Phase contrast (right) and fluorescence (left) images of *Ate1*^{-/-} cells transfected with wild-type (Met) or permanently arginylated (Arg) β -actin constructs. **(Right)** Quantification of the ratios of cell area and lamella length between cells transfected with permanently arginylated (Arg) and wild type β -actin (Met).



Scale bar, 10 μ m. See also fig. S5 for construct details and videos S5 to S7 for the phenotype restoration seen in a single cell (video S5), a single cell moving next to an untransfected cell (video S6), and a cell moving in a monolayer during a wound healing assay (video S7).

Fig. 5. Model of the role of arginylation in actin polymerization and in vivo assembly of intracellular actin networks. **(A)** Structure of bovine β -actin (downloaded from the CN3D structure database at www.ncbi.nlm.nih.gov, accession number 1HLU), with the arginylatable N-terminal Asp3 highlighted in yellow. **(B)** 2D structural model of an actin filament assembled in vitro from the monomers shown on the left, according to the model of actin polymerization by Lorenz *et al.* (19). Every fifth subunit in the filament is labeled with N-terminal Arg. **(C)** Structural model of actin filaments assembled from nonarginylated actin (top) or from a mixture of arginylated and non-arginylated actin in the ratio of 4:1. Filaments in the presence of Arg contain bulky charged groups of Arg residues on the surface that may prevent their side-to-side aggregation. **(D)** (Left) In a wild-type cell (+/+), arginylation of β -actin at the leading edge prevents filaments from aggregation, allowing the formation of a loose network; the absence of arginylation of γ -actin in the cell body allows the tight arrangement of the stress fibers. (Right) In the absence of arginylation (-/-), the β -actin filaments at the leading edge collapse into aggregates, causing the collapse of the lamella and the accumulation of the actin aggregates in the cell body. The γ -actin stress fibers remain unchanged (see also Fig. 3A for real cell images).



segregated, with γ -actin found predominantly in the stress fibers and β -actin predominantly at the leading edge (16–18). Because β -actin is arginylated to about 40% and γ -actin is not, the difference between β - and γ -actin-containing filaments in vivo should be quite substantial. Indeed, at the leading edge, β -actin-containing filaments are assembled from about 40% of arginylated subunits, which should prevent their side-to-side aggregation and induce the formation of a loose network, normally seen at the leading edge of locomoting cells. At the same time, the arrangement of arginylation-free γ -actin-containing filaments in the cell body favors the tightly packed stress fibers (Fig. 5D). Although other protein factors undoubtedly participate in this arrangement, the absence of arginylation in such cells should lead to bundling of β -actin at the leading edge, which would conceivably result in lamella collapse and the accumulation of β -actin aggregates in the cytoplasm, as seen in the *Ate1*^{-/-} cells.

To further test these predictions, we have developed a mathematical model of actin assembly in vitro and in vivo in the presence and absence of arginylation (supporting online material). This model, in agreement with the experimental data and data from the literature, suggests that both β -actin arginylation and its targeting to the leading edge are essential to differentiate between actin isoform-specific networks in vivo and facilitate lamella formation in locomoting cells. The model also predicts that the effect of arginylation on actin assembly can be expected in a range of percentages of arginylated subunits as compared to nonarginylated ones, with effects that are substantial even when as little as 20% of the leading-edge actin is arginylated. Thus, our crude estimation of 40% arginylated β -actin does not need to be accurate to explain the observed effects in vivo and in vitro. In fact, the percentage of arginylated actin should vary in vivo, depending on the motile state of the cell.

Cell motility is critically important during cardiovascular development and angiogenesis. Our finding provides insights into the molecular events that lead to the impairment of these developmental events in *Ate1*^{-/-} mice. Indeed, the defects in lamella formation observed in the *Ate1*^{-/-} cells could result in reduced migration of the cells of cardiovascular lineages. Arginylation has been suggested to regulate many proteins; thus, other protein targets are likely to be responsible for additional arginylation defects on the molecular, cellular, and organismal levels.

References and Notes

- H. Kaji, G. D. Novelli, A. Kaji, *Biochim. Biophys. Acta* **76**, 474 (1963).
- H. Kaji, *Biochemistry* **7**, 3844 (1968).
- E. Balzi, M. Choder, W. N. Chen, A. Varshavsky, A. Goffeau, *J. Biol. Chem.* **265**, 7464 (1990).
- Y. T. Kwon *et al.*, *Science* **297**, 96 (2002).
- P. A. Rubenstein, D. J. Martin, *J. Biol. Chem.* **258**, 3961 (1983).
- P. A. Rubenstein, D. J. Martin, *J. Biol. Chem.* **258**, 11354 (1983).

- D. J. Martin, P. A. Rubenstein, *J. Biol. Chem.* **262**, 6350 (1987).
- D. R. Sheff, P. A. Rubenstein, *J. Biol. Chem.* **264**, 11491 (1989).
- S. Schmitz *et al.*, *J. Mol. Biol.* **295**, 1201 (2000).
- E. S. Hennessey, D. R. Drummond, J. C. Sparrow, *Eur. J. Biochem.* **197**, 345 (1991).
- P. A. Rubenstein, J. A. Spudich, *Proc. Natl. Acad. Sci. U.S.A.* **74**, 120 (1977).
- A. Bachmair, D. Finley, A. Varshavsky, *Science* **234**, 179 (1986).
- J. A. Cooper, T. D. Pollard, *Methods Enzymol.* **85**, 182 (1982).
- J. A. Cooper, S. B. Walker, T. D. Pollard, *J. Muscle Res. Cell Motil.* **4**, 253 (1983).
- K. C. Holmes, M. Tirion, D. Popp, M. Lorenz, W. Kabsch, R. A. Milligan, *Adv. Exp. Med. Biol.* **332**, 15 (1993).
- J. Condeelis, R. H. Singer, *Biol. Cell* **97**, 97 (2005).
- C. A. Otey, M. H. Kalnoski, J. L. Lessard, J. C. Bulinski, *J. Cell Biol.* **102**, 1726 (1986).
- D. Hofer, W. Ness, D. Drenckhahn, *J. Cell Sci.* **110**, 765 (1997).
- M. Lorenz, D. Popp, K. C. Holmes, *J. Mol. Biol.* **234**, 826 (1993).
- We are grateful to I. Sorokina from Midwest Bio Services for the original observation of the arginylated β -actin peptide and helpful suggestions throughout the project;

S. Zigmund, J. Pehrson, and V. Rodionov for helpful discussions; D. Dong for assistance in preparation of the arginylated actin database; B. He from W. Guo's lab for his help with setting up the actin polymerization assays and a gift of recombinant VCA; Y. Wolf for his help with the analysis of the actin crystal structure and preparation of Fig. 5; M. Crawford and the staff of the W. M. Keck Facility at Yale for help with the analysis of actin samples; and S. Zigmund for critical reading of the manuscript. This work was supported by grant PC040372 from the U.S. Department of Defense Congressionally Directed Medical Research Programs to A.K. and by NIH grant P41 RR11823-09 to J.R.Y.

Supporting Online Material

www.sciencemag.org/cgi/content/full/1129344/DC1
Materials and Methods
SOM Text
Figs. S1 to S5
Table S1
References
Videos S1 to S7

13 March 2006; accepted 24 May 2006

Published online 22 June 2006;

10.1126/science.1129344

Include this information when citing this paper.

Massive-Star Supernovae as Major Dust Factories

Ben E. K. Sugerman,^{1*} Barbara Ercolano,² M. J. Barlow,² A. G. G. M. Tielens,³ Geoffrey C. Clayton,⁴ Albert A. Zijlstra,⁵ Margaret Meixner,¹ Angela Speck,⁶ Tim M. Gledhill,⁷ Nino Panagia,¹ Martin Cohen,⁸ Karl D. Gordon,⁹ Martin Meyer,¹ Joanna Fabbri,² Janet. E. Bowey,² Douglas L. Welch,¹⁰ Michael W. Regan,¹ Robert C. Kennicutt Jr.¹¹

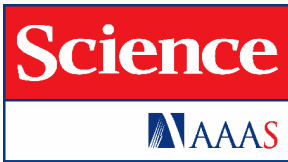
We present late-time optical and mid-infrared observations of the Type II supernova 2003gd in the galaxy NGC 628. Mid-infrared excesses consistent with cooling dust in the ejecta are observed 499 to 678 days after outburst and are accompanied by increasing optical extinction and growing asymmetries in the emission-line profiles. Radiative-transfer models show that up to 0.02 solar masses of dust has formed within the ejecta, beginning as early as 250 days after outburst. These observations show that dust formation in supernova ejecta can be efficient and that massive-star supernovae could have been major dust producers throughout the history of the universe.

Millimeter observations of high-redshift ($z > 6$) quasars have revealed the presence of copious amounts of dust when the universe was as young as 700 million years (1). At the present day, dust in the interstellar medium of the Milky Way and other galaxies is generally thought to be injected mainly by the gentle winds of low-mass stars when they evolve onto the Asymptotic Giant Branch (2). However, stellar-evolution time scales of these low- to intermediate-mass stars are too long for them to have been a major contributor to the dust budget in the early universe (3). Instead, dust in the early universe must reflect the contribution from rapidly evolving (1 to 10 million years) massive stars, which return their nuclear ashes in explosive Type II supernova (SN) events. Theoretical studies have long suggested that dust can condense in the ejecta from core collapse (e.g., Type II) SNe (4), and calculations predict condensation of 0.08 to 1 solar mass (M_{\odot}) of

dust within a few years, depending on metallicity and progenitor mass (5–7). There is also evidence for the origin of some dust in Type II

¹Space Telescope Science Institute, 3700 San Martin Drive, Baltimore, MD 21218, USA. ²Department of Physics and Astronomy, University College London, Gower Street, London WC1E 6BT, UK. ³Kapteyn Astronomical Institute, Post Office Box 800, 9700 AV Groningen, Netherlands. ⁴Department of Physics and Astronomy, Louisiana State University, Baton Rouge, LA 70803, USA. ⁵School of Physics and Astronomy, University of Manchester, Post Office Box 88, Manchester M60 1QD, UK. ⁶Department of Physics and Astronomy, University of Missouri, 316 Physics, Columbia, MO 65211, USA. ⁷Department of Physics, Astronomy, and Maths, University of Hertfordshire, Hatfield AL10 9AB, UK. ⁸Monterey Institute for Research in Astronomy, 200 Eighth Street, Marina, CA 93933, USA. ⁹Steward Observatory, University of Arizona, 933 North Cherry Avenue, Tucson, AZ 85721, USA. ¹⁰Department of Physics and Astronomy, McMaster University, Hamilton, Ontario L8S 4M1, Canada. ¹¹Institute of Astronomy, University of Cambridge, Madingley Road, Cambridge, CB3 0HA, UK.

*To whom correspondence should be addressed. E-mail: sugerman@stsci.edu



Supporting Online Material for
Arginylation of Beta Actin Regulates Actin Cytoskeleton and Cell Motility

Marina Karakozova, Marina Kozak, Catherine C. L. Wong, Aaron O. Bailey, John R. Yates III, Alexander Mogilner, Henry Zebroski, Anna Kashina*

*To whom correspondence should be addressed. E-mail: akashina@vet.upenn.edu

Published 22 June 2006 on *Science* Express
DOI: 10.1126/science.1129344

This PDF file includes:

Materials and Methods
SOM Text
Figs. S1 to S5
Table S1
References

Other Supporting Online Material for this manuscript includes the following:
(available at www.sciencemag.org/cgi/content/full/1129344/DC1)

Videos S1 to S7

Karakozova et al. “Arginylation of beta actin regulates actin cytoskeleton and cell motility”: Supplemental Online Material

Materials and Methods

1. Protein fractionation and metabolic stability assays.

Two-dimensional gel electrophoresis was performed as described in[1] by Kendrick Labs, Inc. (Madison, WI). Actin immunoprecipitation to identify actin isoforms and analyze actin-binding proteins was performed by incubation of whole cell lysates with polyclonal actin antibody (Cytoskeleton, Inc., Denver, CO) or polyclonal antibody against the N-terminal peptide of beta actin (Sigma, St. Louis, MO), followed by coupling to Protein G agarose, pelleting, resuspension in SDS sample buffer, and fractionation on 1D or 2D gel electrophoresis for mass spectrometry analysis of actin-binding proteins or actin isoforms, respectively. Cycloheximide chase of total actin was performed as described in[2] for RGS4 degradation assays. Pulse chase analysis of beta actin was performed by pulse label of cultured cells with ³⁵S-Met/³⁵S-Cys, followed by a chase in non-radioactive media as described in[3]. Cell were lysed at 0, 1.5, 3, and 6 hrs, and equal amounts of cell lysates were treated with anti-beta actin (Sigma), followed by precipitation with protein G agarose and visualization by autoradiography.

2. Peptide synthesis.

Peptides were synthesized in collaboration with the Proteomics Resource Center, Rockefeller University, New York, NY. All peptides were created using a SYMPHONY™ multiple peptide synthesizer (Protein Technologies, Tucson, AZ) on Wang resin (Bachem, King of Prussia, PA) using Fmoc protected amino acids (Anaspec,

San Jose, CA) [4]. Coupling reactions were conducted using 0.3 M HBTU or HATU/HOBT and 0.4 M NMM or 0.6M DIPEA in NMP (N-methylpyrrolidinone) as the primary solvent [5]. Simultaneous resin cleavage and side-chain deprotection were achieved by treatment with concentrated, sequencing grade, trifluoroacetic acid with triisopropylsilane, water, and also ethanedithiol in a ratio of 95:2:2:1 for a 3-6 hour time frame. Rotary evaporation followed by high vacuum overnight was used to remove TFA from the resin bound peptides. Peptides were then released in 8 M acetic acid, filtered from resin, the acidic mixture evaporated, and redissolved in HPLC grade water for lyophilization. All crude lyophilized products were subsequently analyzed by reversed-phase HPLC (Waters Chromatography, Milford, MA) using a Merck Chromolith™ Performance C18 column. Individual peptide integrity was verified by matrix-assisted laser desorption ionization (MALDI) mass spectrometry using a PerSeptive/Applied Biosystems Voyager™ (PE/ABI, Foster City, CA) delayed extraction spectrometer system [6].

3. Single reverse-phase (RP) liquid chromatography, mass spectrometry and database searching.

The cut gel pieces were washed by Milli-Q water and 1:1 mixture of water/acetonitrile, destained by pure acetonitrile and 100 mM ammonium bicarbonate (Sigma), reduced and alkylated with 10 mM Tris(2-carboxyethyl)phosphine hydrochloride (TCEP, Roche Applied Science, Palo Alto, CA) and 55 mM iodoacetamide (IAM, Sigma) in 100 mM ammonium bicarbonate. In-gel digestion was performed in the presence of 50 mM ammonium bicarbonate and 5 mM calcium chloride (Sigma) using sequencing grade soluble trypsin (Promega, Madison, WI) or endoproteinase Lys-C

(Roche Diagnostics, Indianapolis, IN). The resulting peptides were extracted by 5% formic acid and re-dissolved into buffer A (5% acetonitrile with 0.1% formic acid) prior to the LC-MS/MS analysis. Peptide mixtures were pressure-loaded onto a reversed-phase (RP) column and eluted with a linear gradient of acetonitrile (5-80%). Synthetic peptides were dissolved in water and supplemented with 1% formic acid to the final concentration of 100 fmol μl^{-1} and analyzed under the same LC-MS/MS conditions as those used for the real actin sample.

Data-dependent tandem mass spectrometry (MS/MS) analysis was performed in a LTQ-Orbitrap mass spectrometer (Thermo Electron, San Jose, CA). Full MS spectra were acquired by the precursor ion scan using the Orbitrap analyzer with resolution set at 60,000, followed by three MS/MS events in linear ion trap (LTQ), sequentially generated on the first, second and third most intense ions selected from the full MS spectrum. MS scan functions and HPLC solvent gradients were controlled by the Xcalibur data system (Thermo Electron). Tandem mass spectra were searched against two databases, one containing mouse sequences downloaded from EBI-IPI on May 10, 2005, and the other containing arginylated actin variants where Arg was added sequentially onto every Asp, Glu, Cys, Asn (modified to Asp), and Gln (modified to Glu) residue in the actin sequence, using the SEQUEST[7] algorithm. The validity of peptide/spectrum matches was assessed using the SEQUEST-defined parameters, cross-correlation score (XCORR), and normalized difference in cross-correlation scores (DeltaCn). Spectra/peptide matches were only retained if they had a DeltaCn of at least 0.08 and minimum XCORR of 1.8 for +1, 2.5 for +2, and 3.5 for +3 spectra. DTASelect[8] with and without modification for N-terminal arginylation, as described[7] was used to select and sort peptide/spectrum

matches passing this criteria set. Proteins were considered detected if they were identified by at least three spectra passing all of the selection criteria or with at least 10% sequence coverage.

4. Densitometry of actin spots and estimation of the amount of arginylated actin

To estimate the amount of arginylated actin from the gel shown in Fig. 1C of the manuscript, we used Region Statistics tool of the Metamorph Imaging software (Molecular Devices). Each of the three spots marked in Fig. 1C was circled, and protein amount (PA) in the spot was calculated as total area multiplied by total intensity of the spot. To estimate the gel shift, PA values for spots 2 and 3 in the *Ate1*^{-/-} gel were subtracted from the PA values for those spots in WT gel, the resulting numbers were summed, and the percentage of the sum from the total PA in spots 1, 2, and 3 in the WT gel was calculated. We found it to be 19%, which served as the estimation of the ‘approximately 20%’ reported in the paper.

5. Actin polymerization assays

Actin polymerization assays in cell extracts were carried out as described in [9,10]. Cell monolayers were scraped off and resuspended in cold IP buffer (10 mM HEPES, pH 7.1, 2 mM EGTA, 2 mM MgCl₂, 10 mM NaCl, 135 mM KCl, plus protease inhibitors (Sigma, Cat #P8340)), followed by sonication, clarification by centrifugation at 10,000g for 15 min, and high speed centrifugation at 100,000g for 40 min at 4°C. Protein concentration in the supernatants was measured using Bradford assay and adjusted to 1 mg/ml for the polymerization assays. Polymerization was measured by addition of pyrenyl labeled G-actin (Cytoskeleton, Inc.) to the cell extracts alone or supplemented

with seeds prepolymerized from rabbit skeletal muscle actin, or 4 nM of recombinant VCA (referred to in the text as ‘recombinant activator of the actin nucleator complex Arp2/3’), and visualized by pyrenyl fluorescence measured over time, following the method of [11]. Spontaneous polymerization in the extracts for microscopic visualization of actin filaments was performed by incubation of the high speed cell supernatants for 1 hr at room temperature, followed by addition of Rhodamine-phalloidin (Sigma) for 20 min and visualization in the fluorescence microscope, following the procedure described in [10]. Pre-polymerized Rhodamine-phalloidin-labeled actin for the experiments shown in Fig. 2C, bottom) was prepared by 1 hr incubation of rabbit skeletal actin (Cytoskeleton, Inc.) in actin polymerization buffer, followed by addition of Rhodamine-phalloidin for 20 min, and centrifugation at 100,000g for 40 min at 37°C (to wash off unbound phalloidin). Labeled filaments were resuspended in Ate1^{-/-} high speed cell extracts and incubated for 1 hr at room temperature for direct comparison with actin filaments in spontaneously polymerized Ate1^{-/-} extracts (shown in Fig. 2C, middle). By our estimation, the surface properties of non-arginylated muscle actin (containing N-terminally acetylated CDE sequence resulting in a mild negative surface charge) are sufficiently similar to beta and gamma actin found in cultured fibroblasts (a mixture of N-terminally acetylated DDD and EEE) to perform such comparison.

6. Cell culture, imaging and measurements

Immortalized wild type and Ate1^{-/-} fibroblasts were obtained as described in [12]. For wound healing experiments, cells were grown to a dense monolayer, followed by scraping off a portion of the monolayer and observation of the cells moving into the resulting ‘wound’. Measurements of cell volume and area were performed using the

integrated morphometry analysis module of the Metamorph imaging software (Molecular Devices) by analyzing the total area occupied in multiple fields of view by spherical trypsinized cells in suspension (to estimate cell volume) or cultured on the coverslips (to estimate the area of the spread cells). For cell volume measurements, volume (v) was calculated by measuring the diameters of spherical trypsinized cells using the formula $v=4/3\pi r^3$ (where $r=1/2 \times$ cell diameter). Lamella length was determined using the trace feature in Metamorph software, by calculating the length of the line tracing the length of the lamella, determined either as the optically dense line at the edge of the cell in phase contrast images or as the area of beta actin enrichment at the leading edge in immunofluorescence images of beta actin staining.

7. Phenotype rescue experiments

Expression constructs of wild type and ‘permanently arginylated’ beta actin were made using ubiquitin fusion technique[13] by in-frame fusion of cDNAs encoding mouse ubiquitin, wild type or modified beta actin, and EGFP in the pEGFP-N1 vector backbone (Clontech) (see Fig S5 below for the schematic representation of the constructs). Expression of actin-GFP fusion and cotranslational removal of ubiquitin was verified by checking the size of the expressed protein by immunoblotting extracts from the transfected cells with anti-GFP antibody (Roche). Transfection was performed using Lipofectamine plus reagent (Invitrogen) according to the product manual. Both constructs showed high expression levels in transfected cells, which precluded accurate visualization of their intracellular localization above the high fluorescence background, however an enrichment of fluorescence was always seen in the ruffling area of the

leading lamella, as seen in Fig. 4 and the first frames of the Supplementary Videos 5-7. These areas were used for the lamella measurements shown on Fig. 4.

Mathematical model of actin dynamics *in vitro* and *in vivo*

1. Model summary

Quantitative data on the effects of arginylation is sparse and relevant biophysical data is non-existent, so we use theoretical biophysical estimates and mathematical modeling to formulate a semi-quantitative model of how actin dynamics is regulated by arginylation. First, we hypothesize that non-arginylated actin filaments rapidly form bundles due to the counter-ion-induced attraction between negatively charged fibers [14] [15] [16], hence, non-arginylated F-actin aggregates. We argue that ‘bulky’ Arg residues at the sides of actin filaments prevent this bundling. Next, we simulate on the computer *in vitro* F-actin assembly from G-actin and kinetics of F-actin bundling assuming constant rates of second order reactions of polymerization and bundling, and of first order reactions of unbundling and depolymerization. The simulations demonstrate that just by changing the effective bundling rate, the equilibrium is switched from no actin aggregates at all at low bundling rates to significant concentration of aggregates, greater than that of filamentous actin, for moderate bundling rates (Fig S1). The predicted time series of actin assembly and aggregation (Fig S1) are qualitatively very similar to those observed (Fig 2B) rendering credibility to the model.

Next, we simulated spatially distributed lamellipodial densities of F-actin and actin aggregates in the motile cells. We assumed, in addition to the assumptions about the actin kinetics, that G-actin diffuses in the cytoplasm and that both F-actin and actin

aggregates undergo retrograde flow *in the steadily moving cell framework*. Simulations of this spatially distributed model demonstrate that when β -actin is arginylated, density of aggregates is negligible (Fig S2A,B). Notably, when a source of β -actin is localized to the leading edge of the cell, the F-actin also concentrates to the front (Fig S2A, S3A), in agreement with the data (Fig 3A). Interestingly, when there is no source of β -actin at the leading edge, F-actin also fails to localize to the leading edge (Fig S2B, S3B): it is distributed more evenly throughout the lamellipod, and is actually increased at the rear, near the cell body, in agreement with the experimental images (Fig 4). When β -actin is not arginylated, the simulations show that the aggregated actin density becomes greater than that of F-actin (Fig S2C,D). Most of actin is at the rear (Fig S2C,D, S3C,D), with some at the front, when β -actin is targeted to the leading edge (Fig S2C, S3C,D). When there is no source of β -actin at the leading edge, all actin is ‘swept’ to the rear (Fig S2D). These theoretical conclusions also correlate very well with the micrographs (Fig 3A, C).

Thus, the mathematical model generates multiple results that are in good semi-quantitative agreement with the data, which suggests the following simple hypothesis about the mechanism of arginylation role in regulation of actin dynamics. Bulky Arg residues decrease the rate of counter-ion-mediated bundling of actin filaments resulting in dense, isotropic lamellipodial F-actin network at the leading edge and rapid and stable protrusion. Both β -actin localization to the leading edge, and arginylation are necessary for effective lamellipodial protrusion: without the former, though the F-actin does not aggregate, the density of the F-actin network at the leading edge is too low. Without the latter, much of actin aggregates and again the F-actin network at the leading edge is too weak.

2. Kinetics of counter-ion-induced bundle formation of F-actin

Electrostatic effect of arginylation is likely negligible, because positive charge on Arg is too small with great negative charge density on actin. However, ‘bulkiness’ of Arg is the key factor: calculations in [3] demonstrate that the free energy of electrostatic interaction between two actin filaments becomes negative only at very small, nm-range distances between the filaments. This means that the filaments attract and can bundle only when they are in very close proximity. Arg residue creates effective steric repulsion – it prevents side-to-side touching of the filaments keeping them at distances not less than ~ 1 nm from each other, which would reduce the effective bundling rate by an order of magnitude [2,3].

The fact that roughly a quarter of actin subunits are arginylated is probably not coincidental: F-actin is a double helix with the twist of 37 nm. Thus, if every fourth subunit is arginylated, then there is an Arg residue on the average per every $\sim 25^\circ$ angular interval $((5.4\text{nm}/37\text{nm})\cdot 180^\circ$, where 5.4 nm is the size of G-actin) around the filament, providing effective steric repulsion at any angle of collision between filaments in the cytoplasm. (Rough estimate is that the bulky residues ~ 1 nm in size should be placed at least per every 30° intervals around cylindrical filaments of radius ~ 5.4 nm in order for the filaments sides not to touch each other.) At the same time, most of the actin subunits are not arginylated, and their interactions with a host of actin binding proteins is not altered. Smaller fraction of arginylated actin would lead to less effective anti-bundling effect: just twice fewer arginylated subunits would mean that there is an Arg residue on the average per every $\sim 50^\circ$ angular interval around the filament, which will lead to possibility of close proximity of filaments’ sides and subsequent bundling.

3. Model of *in vitro* assembly and aggregation of F-actin

We describe the system with time-dependent concentrations of actin filaments, $f(t)$, and of actin aggregates, $a(t)$ (both densities are scaled to the corresponding number of actin subunits). We describe the dynamics of actin with the system of ordinary differential equations:

$$\begin{aligned}
 \underbrace{\frac{df}{dt}}_{\text{F-actin dynamics}} &= \underbrace{rfg}_{\text{assembly}} - \underbrace{\gamma_1 f}_{\text{disassembly}} - \underbrace{k_1 af}_{\text{bundling}} + \underbrace{k_2 a}_{\text{unbundling}} \\
 \underbrace{\frac{da}{dt}}_{\text{aggregate dynamics}} &= \underbrace{rag}_{\text{assembly}} - \underbrace{\gamma_2 a}_{\text{disassembly}} + \underbrace{k_1 af}_{\text{bundling}} - \underbrace{k_2 a}_{\text{unbundling}} \\
 g &= A - f - a
 \end{aligned} \tag{1}$$

Here r is the effective constant rate of polymerization. We assume that there is a characteristic average size of actin filaments, so the number of barbed and pointed ends is proportional to the respective densities. The net rate of the assembly is proportional to the F-actin/aggregate density (and to corresponding number of the barbed ends), and to the G-actin density, g . The latter is equal to the total conserved actin concentration, A , minus the concentration of assembled subunits. The F-actin/aggregates disassemble with the constant rates γ_1, γ_2 , respectively. We assume that $\gamma_1 > \gamma_2$: aggregates disassemble slower due to steric hindrance for subunits detachment from the pointed ends in the aggregates. We further assume that the individual filaments unbundled from the aggregates at constant rate k_2 , and that the net bundling rate is diffusion limited [3] and is proportional to the densities of individual filaments and aggregates; k_1 is the corresponding proportionality coefficient.

We non-dimensionalize the model by using $1/\gamma_1$ as the time scale, A as the scale of densities, and by substituting expression for g into the first two equations:

$$\begin{aligned}
 \underbrace{\frac{df}{dt}}_{\text{F-actin dynamics}} &= \underbrace{\varepsilon_1 f(1-f-a)}_{\text{assembly}} - \underbrace{f}_{\text{disassembly}} - \underbrace{\varepsilon_2 af}_{\text{bundling}} + \underbrace{\varepsilon_3 a}_{\text{unbundling}} \\
 \underbrace{\frac{da}{dt}}_{\text{aggregate dynamics}} &= \underbrace{\varepsilon_1 a(1-f-a)}_{\text{assembly}} - \underbrace{\gamma a}_{\text{disassembly}} + \underbrace{\varepsilon_2 af}_{\text{bundling}} - \underbrace{\varepsilon_3 a}_{\text{unbundling}}
 \end{aligned} \tag{2}$$

The system behavior depends on four dimensionless combinations of parameters: rescaled assembly rate $\varepsilon_1 = rA/\gamma_1$, bundling/unbundling rates $\varepsilon_2 = k_1A/\gamma_1$ and $\varepsilon_3 = k_2A/\gamma_1$, and the ratio of aggregate to F-actin disassembly rates $\gamma = \gamma_2/\gamma_1$. The values of the parameters are unknown; we choose them so that the ratio of G- to F-actin is reasonable and that bundling/unbundling processes take place on the same time scales as assembly/disassembly. Qualitatively, the model results are robust to varying the parameters. We simulate the equations (2) with initial conditions $f = 0.15, a = 0.0001$ (initial number of bundles is negligible), $\varepsilon_1 = 1.5, \varepsilon_3 = 0.7, \gamma = 0.3$, and varying the bundling rate ε_2 . The simulation results are shown in Fig S1A,B. At small bundling rate ($\varepsilon_2 = 0.2$ in the shown result), the aggregate density remains negligible, while the F-actin density exponentially saturates to the equilibrium (Fig S1A). At large bundling rate ($\varepsilon_2 = 2$ in the shown result), the aggregate density remains small for a finite time, while the F-actin density exponentially saturates, but then the bundling density increases rapidly to a steady value, while the F-actin density synchronously drops (Fig S1B), resembling the observed dynamics.

We also used Monte Carlo stochastic simulations to vividly illustrate the *in vitro* behavior (Fig. 1 C,D). In the simulations, actin filaments and bundles appear and disappear according to the same dynamics as that underlying the deterministic model described above. All actin is allowed to diffuse rapidly; bundling takes place when the filaments collide with bundles. Bundles split in two when they ‘accumulate’ critical number of filaments, while filaments split in two when they ‘grow’ beyond a threshold. The rates are scaled so that the overall concentrations follow the behavior predicted by the deterministic model.

4. Model of *in vivo* dynamics of actin in lamellipodia of motile cells

In order to elucidate spatial-temporal actin dynamics in motile cells, we make a number of simplifying approximations. A full scale 2D model of the lamellipod is too computationally intensive, and we do not have sufficient knowledge to make such model of a complex cell adequate [17], so we limit ourselves to a simple 1-dimensional model that represents an anterior-posterior transect of the lamellipod. We also assume that the locomotion is steady: the lamellipod has a constant length, and in the framework of the motile cell F-actin undergoes steady constant retrograde flow. Thus, we describe the densities of the lamellipodial F-actin, $F(x,t)$, actin aggregates, $A(x,t)$, and G-actin, $G(x,t)$, as functions of time and of the 1D coordinate x ($x=0$ corresponds to the lamellipodial rear, at the cell body, $x=L$ – to the leading edge). We describe the lamellipodial dynamics by the following system of equations (see [17] [18] for detailed discussion of similar models):

$$\begin{aligned}
\underbrace{\frac{\partial F}{\partial t}}_{F\text{-actin dynamics}} &= q(x) \left[\underbrace{rFG}_{\text{assembly}} - \underbrace{k_1 AF}_{\text{bundling}} + \underbrace{k_2 A}_{\text{unbundling}} \right] - \underbrace{\gamma_1 F}_{\text{disassembly}} + V \underbrace{\frac{\partial F}{\partial x}}_{\text{retrograde flow}} \\
\underbrace{\frac{\partial A}{\partial t}}_{\text{aggregate dynamics}} &= q(x) \left[\underbrace{rAG}_{\text{assembly}} + \underbrace{k_1 AF}_{\text{bundling}} - \underbrace{k_2 A}_{\text{unbundling}} \right] - \underbrace{\gamma_2 A}_{\text{disassembly}} + V \underbrace{\frac{\partial F}{\partial x}}_{\text{retrograde flow}} \\
\underbrace{\frac{\partial G}{\partial t}}_{G\text{-actin dynamics}} &= -q(x) \left[\underbrace{r(A+F)G}_{\text{assembly}} \right] + \underbrace{\gamma_1 F + \gamma_2 A}_{\text{disassembly}} + D \underbrace{\frac{\partial^2 G}{\partial x^2}}_{\text{diffusion}} + \underbrace{s(x)}_{\beta\text{-actin source}}
\end{aligned} \tag{3}$$

Here the first four terms in the first two equations are the same as those in the *in vitro* model (1) for corresponding densities, with the following modification: the assembly and bundling/unbundling kinetics depends on the position in the lamellipod. We assume that at the narrow rim of width $w \sim 1 \mu\text{m}$ at the leading edge these processes are the same as in the *in vitro* model ($q(x)=1$ if $L-w < x < L$), while in the bulk of the lamellipod some filaments are capped and/or incorporated into more stable lamellar structure [19], and the respective dynamics are slower ($q(x) < 1$ if $0 < x < L-w$; we use the value $q(x)=0.7$ if $0 < x < L-w$). In the equation for the density of G-actin, the first few algebraic terms balance the assembly/disassembly terms for filamentous actin. To account for the spatial dynamics of actin, we use the spatial derivative terms describing retrograde flow of the filamentous actin with the rate V in the first two equations, and the diffusion term (with constant diffusion coefficient D) in the third equation for G-actin. Finally, we introduce the term $s(x)$ (in the last equation) to describe the source of β -actin targeted to the leading edge [20]: we assume that there is a constant source of β -actin within the rim of width w at the leading edge, and the balancing small sink everywhere else in the lamellipod ($s(x) < S$ if $L-w < x < L$; $s(x) = Sw/(L-w)$ if $0 < x < L-w$).

We non-dimensionalize (3) using the same scales as in (1-2), plus we use the lamellipodial width L as the spatial scale. We use characteristic values $L \sim 10 \mu\text{m}$, $V \sim 0.1 \mu\text{m}/\text{sec}$, $D \sim 5 \mu\text{m}^2/\text{sec}$. For the wild type cells, we use the values above; for the $-/-$ cells, we make both the lamellipodial width and retrograde flow rate twice smaller to account for our observations. We simulate the system of equation (3) using constant non-dimensional densities $G=0.6$, $A=0.1$, $F=0.3$. We vary the β -actin source at the leading edge from $S=0.1$ to 0. We use no flux boundary condition for all actin densities and perform simulations on desktop PC using Matlab and FTCS and downwind numerical algorithms [21].

Figure S2 shows corresponding asymptotically stable steady spatial distribution of actin densities. Figure S3 and movies 1-4 illustrates corresponding spatial-temporal dynamics in radially symmetric lamellipodial ‘wedges’.

Figure legends

Figure S1. Comparison of MS/MS spectra of arginylated actin peptide found in vivo (A) with the synthetic arginylated (B) and acetylated (C) peptides. b, y, and neutral loss ions are annotated in red, blue, and black color, respectively. The inserts on the right show amplified region of the corresponding spectra within the red rectangle. A, RDDIAALVVDNGSGMCK peptide $[M+2H]^{2+}$ (m/z 910.96). B, synthetic peptide RDDIAALVVDNGSGMCK $[M+2H]^{2+}$ (m/z 910.94). (C), synthetic peptide Ac-DDIAALVVDNGSGMCK $[M+2H]^{2+}$ (m/z 910.93).

MS/MS spectrum of the arginylated peptide found in vivo is identical to the synthetic arginylated, but not acetylated peptide by all the identified b ion masses, which in the acetylated peptide differ by approximately 1 Da from both arginylated peptides (see Supplemental Table 1 for the list of masses). In addition, both arginylated peptides share characteristic features of the spectrum which differ from the acetylated peptide, including characteristic b2 and b3 ions predominant in the small mass range of spectrum (absent from the acetylated peptide spectrum) as well as significant y2, y3, y4 and y5 ions characteristic for the small mass range in the acetylated peptide spectrum (not observed in the spectra of both arginylated peptides).

Figure S2. Model of actin polymerization in vitro. A-B: Computed from equations (2) time series for F-actin (dashed) and aggregated actin (solid) densities for arginylated (A) and non-arginylated (B) actin. Time is plotted on the x-axis, density is on the y-axis (both in arbitrary units). C-D: snapshots from the Monte-Carlo simulations of the actin densities for arginylated (C) and non-arginylated (D) actin. Dots are individual filaments, stars are actin aggregates.

Figure S3. Model of actin polymerization in vivo. Computed from equations (3) stable steady spatial distributions F-actin (dashed), aggregated actin (solid) and G-actin (dotted) densities in the cell lamella. Spatial coordinate is plotted on the x-axis (distance from the cell body to the lamella is increasing left to right), density is on the y-axis; both axes are in arbitrary units. A: arginylated actin, β -actin is targeted to the leading edge. B: arginylated actin, β -actin is not targeted to the leading edge. C: non-arginylated actin, β -actin is targeted to the leading edge. D: non-arginylated actin, β -actin is not targeted to the leading edge.

Figure S4. Model of actin polymerization in vivo presented as actin densities shown on 2D lamellipodial ‘wedges’. Dark shading corresponds to high density, light – to low density; distance from the cell body to the leading edge increases left to right. Stars are fiduciary marks on the lamellipodial networks illustrating the retrograde flow in the corresponding movies M1-M4. A: F-actin density for arginylated actin, β -actin is targeted to the leading edge (corresponds to Fig S2A). B: F-actin density for arginylated actin, β -actin is not targeted to the leading edge (corresponds to Fig S2B). C: F-actin density for non-arginylated actin, β -actin is targeted to the leading edge (corresponds to Fig S2C). D: Aggregated actin density for non-arginylated actin, β -actin is targeted to the leading edge (corresponds to Fig S2C). Movies M1—M4 illustrate the events shown in the stationary images S3A-D.

Figure S5. Schematic representation of the expression constructs used for the phenotype rescue experiments. Met indicates Met1 of the beta actin sequence. Arg indicates the arginine residue added to the beta actin sequence in front of the Asp3 to imitate the arginylated form of beta actin. Arrows indicate the cleavage site for ubiquitin-specific proteases that co-translationally remove ubiquitin from the fusion, exposing the N-terminal residue of the fusion.

Supplementary video legends.

Video 1.

Time lapse images of the lamellar activity in a single wild type mouse fibroblast.

Stationary cell was chosen for continuous observation. Cell in the images undergoes global ruffling and contractility in the body, and forms a wide lamella along the cell edge.

Video 2.

Time lapse images of the lamellar activity in a single *Ate1*^{-/-} mouse fibroblast. Cell similar in morphology and behavior to the wild type cell in Video 1 was chosen for comparison of lamella and ruffling activity.

Video 3

Time lapse images of the wild type fibroblast monolayer moving into the wound.

Moving cells form a wide lamella and cover the whole area of the substrate in the field of view over the time course of 8 hrs.

Video 4

Time lapse images of the *Ate1*^{-/-} fibroblast monolayer moving into the wound. Moving cells are unable to form a normal lamella and fail to efficiently cover the entire area of the substrate in the field of view over the time course of 8 hrs.

Video 5

Time lapse images of an *Ate1*^{-/-} fibroblast transfected with 'permanently arginylated' beta actin. The cell forms a wide lamella during movement but continues to exhibit defects in ruffling activity and cortical flow characteristic for the *Ate1*^{-/-} cells.

Video 6

Time lapse images of an Ate1^{-/-} fibroblast transfected with ‘permanently arginylated’ beta actin moving next to an untransfected Ate1^{-/-} fibroblast for comparison. The transfected cell, unlike the untransfected one, forms a wide lamella during movement, indicating that the re-introduction of the arginylated beta actin restores the lamella formation phenotype in Ate1^{-/-} cells.

Video 7

Time lapse images of an Ate1^{-/-} fibroblast transfected with ‘permanently arginylated’ beta actin moving within a monolayer of untransfected Ate1^{-/-} cells during wound healing in culture. The transfected cell, unlike its multiple untransfected neighbors, forms a wide lamella during movement, indicating that the re-introduction of the arginylated beta actin restores the lamella formation phenotype in Ate1^{-/-} cells.

Figure S1

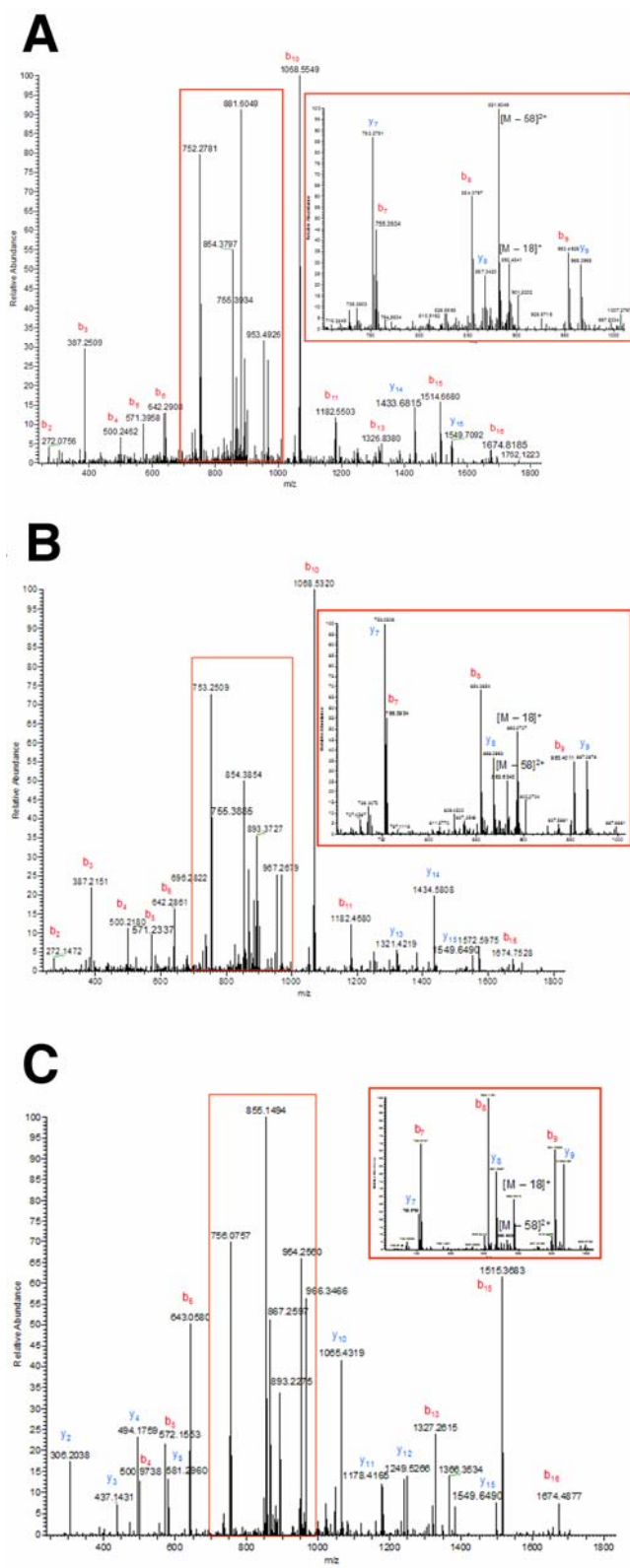


Figure S2

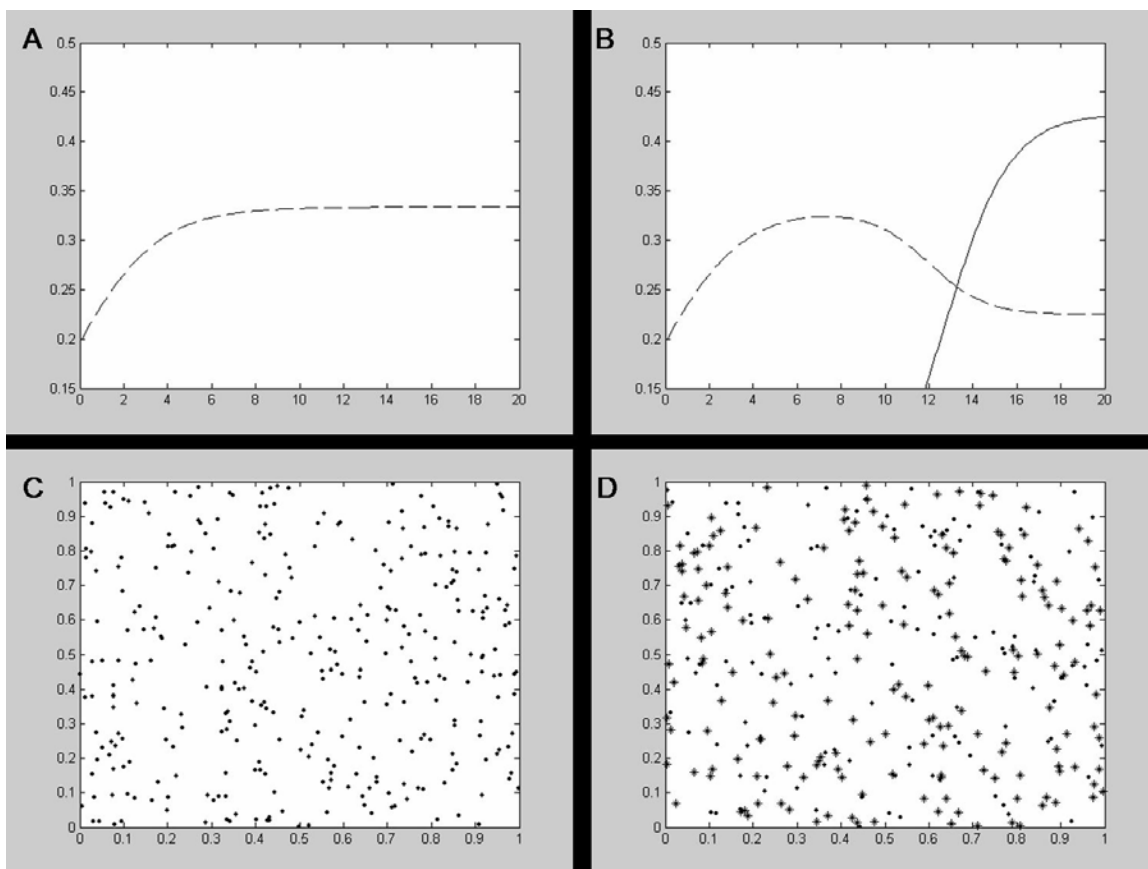


Figure S3

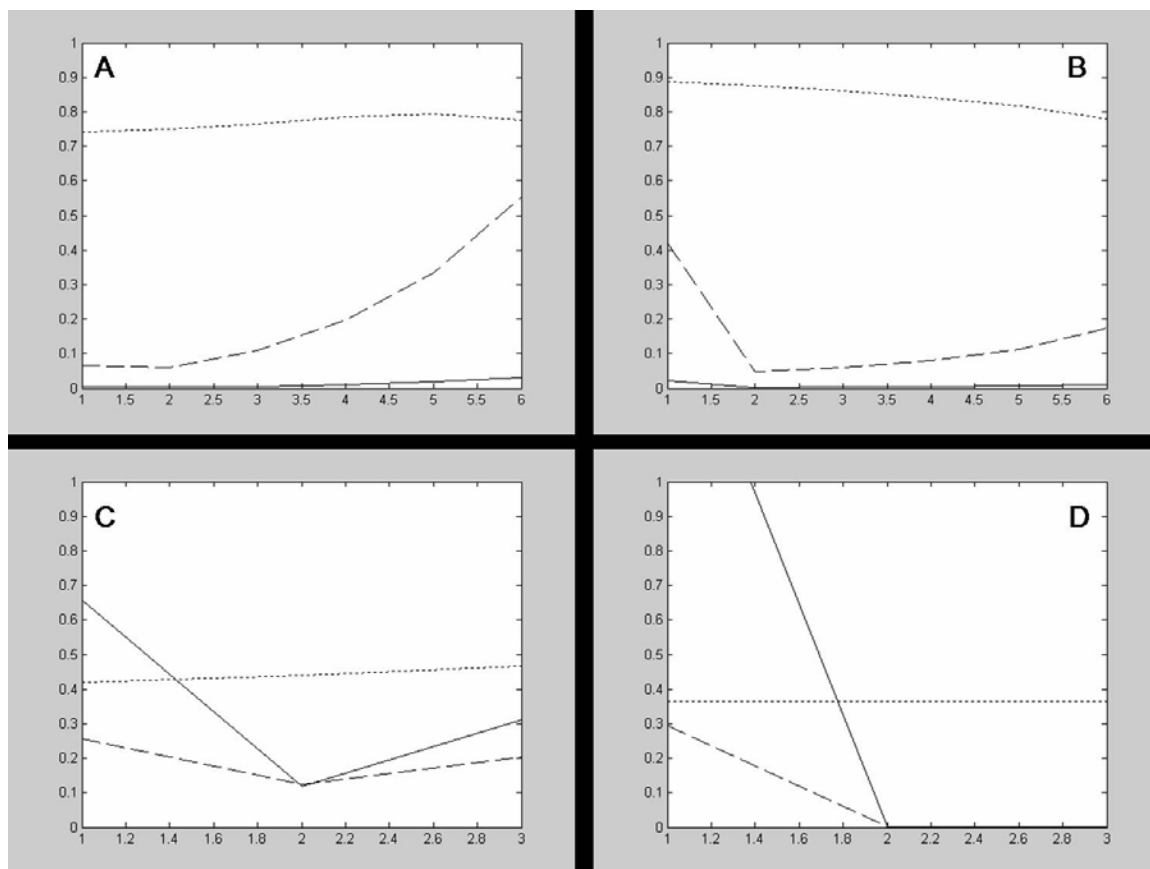


Figure S4

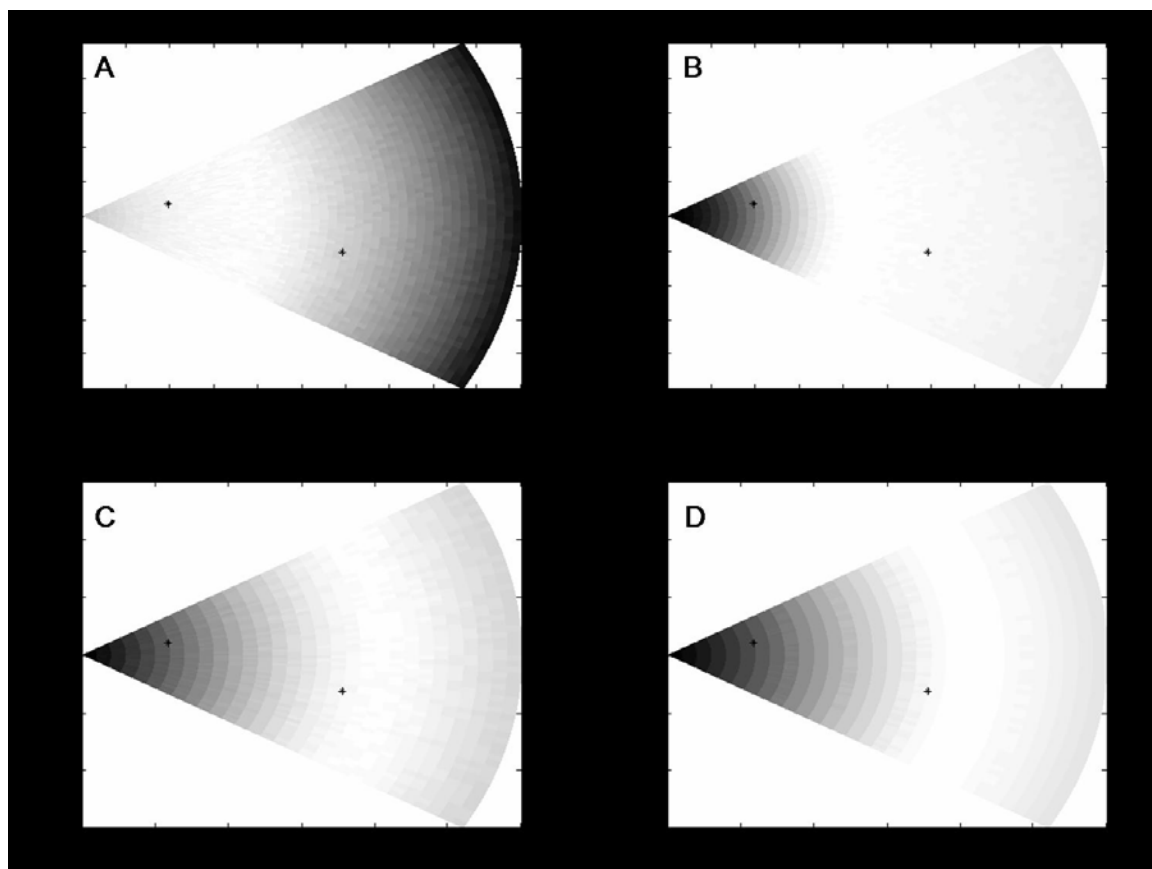
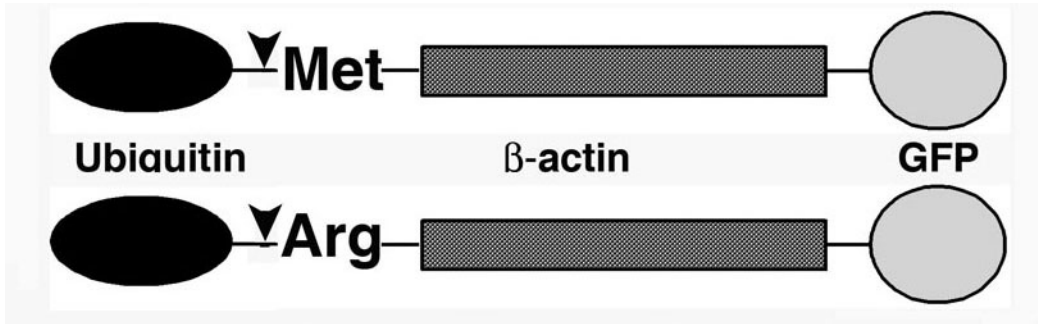


Figure S5



Seq	#	Actin Peptide b ion (observed)	N-terminal Arginylation b ion (theoretical)	N-terminal Acetylation b ion (theoretical)
R	1	-	157.1089	158.0458
D	2	272.0756	272.1359	273.0727
D	3	387.2509	387.1628	388.0996
I	4	500.2462	500.2469	501.1837
A	5	571.3958	571.2840	572.2208
A	6	642.2908	642.3211	643.2579
L	7	755.3934	755.4052	756.3419
V	8	854.3797	854.4736	855.4103
V	9	953.4926	953.5420	954.4788
D	10	1068.5549	1068.5689	1069.5057
N	11	1182.5503	1182.6119	1183.5487
G	12	1239.6405	1239.6333	1240.5702
S	13	1326.838	1326.6654	1327.6022
G	14	1383.8179	1383.6868	1384.6237
M	15	1514.668	1514.7273	1515.6642
C	16	1674.8185	1674.7580	1675.6733
K	17	-	1802.8315	1803.7683

Supplemental Table 1. Comparison of b ion fragment masses for N-terminally arginylated and acetylated peptides to the N-terminally arginylated actin peptide found in vivo.

References

- [1] O'Farrell PH. High resolution two-dimensional electrophoresis of proteins. *J Biol Chem* 1975;250 (10):4007-21.
- [2] Rai R, Kashina A. Identification of mammalian arginyltransferases that modify a specific subset of protein substrates. *Proc Natl Acad Sci U S A* 2005;102 (29):10123-8.
- [3] Kumar KG, Tang W, Ravindranath AK, Clark WA, Croze E, Fuchs SY. SCF(HOS) ubiquitin ligase mediates the ligand-induced down-regulation of the interferon-alpha receptor. *Embo J* 2003;22 (20):5480-90.
- [4] Wellings DA, Atherton E. Standard Fmoc protocols. *Methods Enzymol* 1997;289:44-67.
- [5] Knorr R, Trzeciak, A., Bannwarth, W., & Gillesen, D. D. *Tetrahedron Letters* 1989;30:1927-30.
- [6] Beavis RC, Chait BT. Matrix-assisted laser desorption ionization mass-spectrometry of proteins. *Methods Enzymol* 1996;270:519-51.
- [7] Eng JK, McCormack, A.L., and Yates, J.R., III. An approach to correlate tandem mass spectral data of peptides with amino acid sequences in a protein database. *J Am Soc Mas Spectrom* 1994;5 (11):976-89.
- [8] Tabb DL, McDonald WH, Yates JR, 3rd. DTASelect and Contrast: tools for assembling and comparing protein identifications from shotgun proteomics. *J Proteome Res* 2002;1 (1):21-6.
- [9] Zigmond SH. In vitro actin polymerization using polymorphonuclear leukocyte extracts. *Methods Enzymol* 2000;325:237-54.
- [10] Zigmond SH, Joyce M, Borleis J, Bokoch GM, Devreotes PN. Regulation of actin polymerization in cell-free systems by GTPgammaS and Cdc42. *J Cell Biol* 1997;138 (2):363-74.
- [11] Cooper JA, Walker SB, Pollard TD. Pyrene actin: documentation of the validity of a sensitive assay for actin polymerization. *J Muscle Res Cell Motil* 1983;4 (2):253-62.
- [12] Kwon YT, Kashina AS, Davydov IV, Hu RG, An JY, Seo JW, Du F, Varshavsky A. An essential role of N-terminal arginylation in cardiovascular development. *Science* 2002;297 (5578):96-9.
- [13] Bachmair A, Finley D, Varshavsky A. In vivo half-life of a protein is a function of its amino-terminal residue. *Science* 1986;234 (4773):179-86.
- [14] Tang JX, Janmey PA. The Polyelectrolyte Nature of F-actin and the Mechanism of Actin Bundle Formation
10.1074/jbc.271.15.8556. *J. Biol. Chem.* 1996;271 (15):8556-63.
- [15] Yu X, Carlsson AE. Kinetics of Filament Bundling with Attractive Interactions
10.1529/biophysj.104.047373. *Biophys. J.* 2004;87 (6):3679-89.
- [16] Yu X, Carlsson AE. Multiscale Study of Counterion-Induced Attraction and Bundle Formation of F-Actin Using an Ising-like Mean-Field Model. *Biophys. J.* 2003;85 (6):3532-43.
- [17] Rubinstein B JK, Mogilner A. Multiscale two-dimensional modeling of a motile simple-shaped cell. *SIAM J MMS* 2005;3 (413-439).

- [18] Mogilner A, Edelstein-Keshet L. Regulation of Actin Dynamics in Rapidly Moving Cells: A Quantitative Analysis. *Biophys. J.* 2002;83 (3):1237-58.
- [19] Ponti A, Machacek M, Gupton SL, Waterman-Storer CM, Danuser G. Two Distinct Actin Networks Drive the Protrusion of Migrating Cells
10.1126/science.1100533. *Science* 2004;305 (5691):1782-6.
- [20] Condeelis J, Singer RH. How and why does beta-actin mRNA target? *Biol Cell* 2005;97 (1):97-110.
- [21] Garcia AL. *Numerical Methods for Physics*. Englewood Cliffs NJ: Prentice Hall, 2000.

ejecta. In general, such ejecta are clumpy, and a large fraction of the dust may be in these clumps and be too cold to give rise to mid-infrared emission. Motivated to search for the “missing” dust, and aware of the possible pitfalls in the interpretation of supernovae spectra, Sugerman and co-workers searched for several of the dust-formation signatures in the optical to mid-infrared spectrum of the Type II SN 2003gd in the galaxy NGC 628. SN 2003gd is the first supernova with a confirmed red-giant progenitor. This star’s mass was between 6 and 12 M_{\odot} . Models predict that a star of that mass would eject 0.3 M_{\odot} of refractory elements in a supernova explosion. Collecting data from several epochs, they showed that the optical and mid-infrared spectrum of this supernova showed several telltale signs of dust formation: the appearance of a mid-infrared excess, an increase in the optical extinction, and a blueshifting of the H α emission line. The manifestation of the three signatures provides very compelling evidence that dust has formed in

this supernova about 500 to 680 days after the outburst. They also allow for a comprehensive analysis of the data in order to infer the dust mass. Using a radiative transfer code to simultaneously account for the optical extinction and infrared emission, Sugerman *et al.* conclude that the supernova formed about 0.04 M_{\odot} of dust, about 13% of the mass of dust that could have formed if all refractory elements in the ejecta condensed into dust grains.

The yield of SN 2003gd is the largest found in supernova ejecta thus far, and therefore represents an important milestone in the quest for the origin of interstellar dust. However, the yield still falls short of making supernovae the dominant dust factories required to balance the amount of grain destruction in the interstellar medium, or to account for the mass of dust observed in high-redshift galaxies. If future observations find this to be a typical yield, then scientists will have to take a harder look at other processes that determine the evolution of dust, such as the rate of their destruction in the

general interstellar medium, and the accretion rate in molecular clouds.

References and Notes

1. B. E. K. Sugerman *et al.*, *Science* **313**, 196 (2006); published online 8 June 2006 (10.1126/science.1128131).
2. E. Dwek, *Astrophys. J.* **501**, 643 (1998).
3. A. P. Jones, in *Astrophysics of Dust*, *Astron. Soc. Pac. Conf. Series* 309, A. N. Witt, G. C. Clayton, B. T. Draine, Eds. (Astronomical Society of the Pacific, San Francisco, CA, 2004), p. 347.
4. T. Kosaza, H. Hasegawa, K. Nomoto, *Astrophys. J.* **344**, 325 (1989).
5. F. Cernuschi, F. R. Marsicano, I. Kimel, *Ann. Astrophys.* **28**, 860 (1965).
6. F. Hoyle, N. C. Wickramasinghe, *Nature*, **226**, 62 (1970).
7. D. D. Clayton, *Astrophys. J.* **199**, 765 (1975).
8. D. D. Clayton, L. R. Nittler, *Annu. Rev. Astron. Astrophys.* **42**, 39 (2004).
9. L. B. Lucy, I. J. Danziger, C. Gouiffes, P. Bouchet, in *Supernovae. The Tenth Santa Cruz Workshop in Astronomy and Astrophysics*, S. E. Woosley, Ed. (Springer-Verlag, New York, 1991), p. 82.
10. The author acknowledges support from NASA LISA03.

10.1126/science.1130423

CELL BIOLOGY

Actin Discrimination

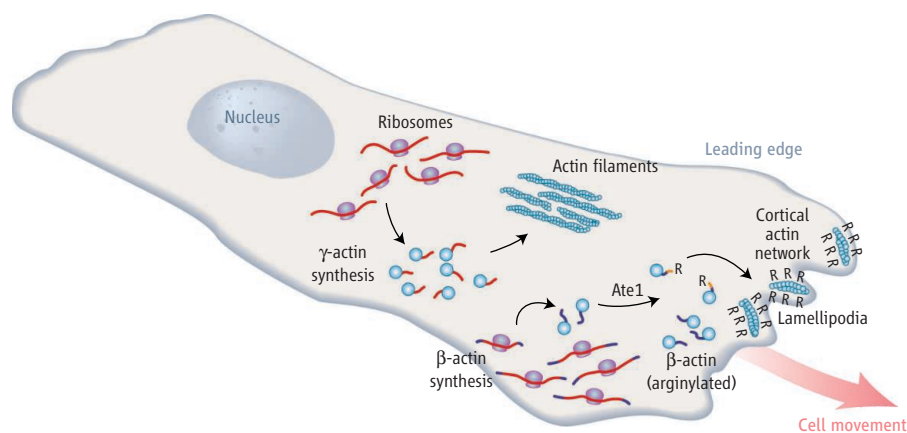
J. Chloë Bulinski

Actin is one of the most abundant proteins in eukaryotic cells. Among its functions, it is one of the main constituents of the cell’s dynamic cytoskeletal infrastructure. It is also highly conserved. From birds to humans, each of the six actin isoforms shares 100% amino acid sequence identity across species, with individual gene products showing tissue-specific, rather than species-specific, sequence differences (1). Within all species, there is an unprecedented sequence conservation between the β and γ isoforms of actin—they differ in only 4 out of their 373 amino acid residues. It has been widely assumed that these isoforms perform distinct functions in the cytoplasm, as evolutionary conservation of protein sequences has been taken to imply functional importance (2). However, data supporting this quite reasonable assumption have been slow in coming. On page 192 of this issue, Karakozova *et al.* (3) put to rest the long-standing puzzle of the simultaneous expression of these nearly identical actin isoforms in nonmuscle cells. Chemical modification of β -actin allows cells to discriminate this isoform and restrict its assembly into higher order actin networks that assist in cell motility.

Although the β and γ isoforms of actin are both expressed in varying amounts in the same tissues throughout an organism (4), the subcellular localization of the messenger RNAs (mRNAs) that encode them—and therefore, their sites of synthesis—are markedly different. β -actin mRNA is concentrated near the very front, or leading edge, of a moving fibroblast cell (see the figure) (5). In contrast, γ -actin mRNA is

Addition of arginine to a type of actin restricts this cytoskeletal protein to the front end of cells where it helps cells to move.

localized throughout the central region of the cell. This finding suggested that newly synthesized β -actin could perhaps find specific binding partners in the broad, actin-filled extensions at the leading edge that enable cells to move (lamellipodia). β -actin could also preferentially interact there with myosin, actin’s force-generating protein partner. In many cases, though, cell size made these notions unsatisfying: Why would



Arginylated actin. β -actin is synthesized at the leading edge of motile fibroblast cells. Some of it is modified with arginine (R). The presence of this bulky moiety on the surface of β -actin filaments restricts its assembly into individual filaments in lamellipodia. In contrast, γ -actin is synthesized in the central region of the cell, is not arginylated, and forms large filament bundles that cannot gain entry to lamellipodia. This segregated synthesis and organization of the two actin isoforms facilitates cell movement.

The author is in the Department of Biological Sciences and the Department of Pathology and Cell Biology, Columbia University, 1212 Amsterdam Avenue, New York, NY 10027–2450, USA. E-mail: jcb4@columbia.edu

these two isoforms not mix, through diffusion, during their residence time in the cytoplasm? After all, their sites of synthesis are, on average, only 1 to 10 μm away from one another, and their turnover time is several days. Besides, even with disparate localizations of β - and γ -actin mRNA synthesis, the conundrum remained: Could the slight differences in their sequences imbue them with differences in function?

The fact that antibodies were generated that specifically recognize the amino-terminal differences between β - and γ -actin (4) raised the possibility that cellular proteins could also exhibit isoform-specific recognition. A few glimmers of suggestive evidence were tantalizing. These two isoforms of actin can form biochemically distinct complexes with the actin-binding protein profilin (6). The actin-binding protein betaCap73 discriminates between nonmuscle β -actin and muscle α -actin, which are more divergent in amino acid sequence than β - and γ -actin (7). However, no binding proteins specific for β - or γ -actin emerged.

That is, until now. Karakozova *et al.* demonstrate recognition of β -actin, but not γ -actin, by the enzyme Ate1 (Arg-tRNA protein transferase 1). Ate1 catalyzes the addition of an arginine residue to the amino terminus of target proteins (8), a modification thought to mark proteins for prompt ubiquitination and proteasome-mediated degradation. As a result, the two actin isoforms are not only chemically different, but the authors further demonstrate that the two isoforms take on wholly different organizations of the filamentous actin (f-actin) in which they are enriched. Arginylated β -actin forms single f-actin filaments, whereas γ -actin forms dense parallel bundles of filaments. The authors also reveal that each isoform's filament organization provides a possible mechanism for maintaining the two actins as separate pools. The leading edge can accommodate a fibrous meshwork of actin filaments, such as that generated by individual filaments of β -actin. More interior to the cell, thick filament bundles of γ -actin prevail, as they are too large to invade the leading edge. Strikingly, at least one of the elusive isoform-specific actin-binding proteins turns out to be actin itself. Actin filaments containing arginylated β -actin appear to repel one another instead of forming bundles.

The mystery of the two isoforms was solved, as is often the case, by investigators seemingly unconcerned by the arcane and long-standing question of actin's molecular evolution. Karakozova *et al.* were sleuthing a mystery of their own: Investigating the N-end rule of protein modification, which relates the half-life of a protein to the identity of its amino-terminal residue (9), led the authors to engineer mice lacking Ate1. The Ate1-deficient mice died during embryogenesis as a result of cardiovascular defects, suggesting that the enzyme plays a vital role in turnover of its substrate proteins.

Surprisingly, although β -actin was identified as a major substrate of Ate1, its isoform-specific arginylation seems to have nothing to do with shortening its half-life. Instead, arginylation of β -actin at its amino terminus—a domain that projects from β -actin filaments (10)—restricts the organization of β -actin filaments, and apparently prolongs the restricted subcellular localization of the β -actin isoform to the lamellipodial region where it was synthesized. The authors demonstrate that preventing arginylation of β -actin in fibroblasts causes inappropriate bundling of β -actin filaments within the cortical actin network (the cytoskeleton that lies just beneath the plasma membrane) at the leading edge, thus contributing to the defects in cell motility.

It is clear from the work of Karakozova *et al.* that posttranslational arginylation of a single protein target can induce global changes on the cellular level. Ate1 is evolutionarily conserved, and there are undoubtedly other substrates whose modification similarly results in altered properties that affect their cellular functions (or their degradation). Does this modification affect

the cardiac muscle α -actin isoform, given that the similarity of its amino terminus to β -actin (2) makes it a possible substrate for Ate1? Is the modification reversible? The answer to one conundrum has, not surprisingly, given rise to many more questions.

References

1. J. Vandekerckhove, K. Weber, *J. Mol. Biol.* **126**, 783 (1978).
2. J. Das, S. T. Miller, D. L. Stern, *Mol. Biol. Evol.* **21**, 1572 (2004).
3. M. Karakozova *et al.*, *Science* **313**, 192 (2006); published online 22 June 2006 (10.1126/science.1129344).
4. C. A. Otey, M. H. Kalnoski, J. C. Bulinski, *J. Cell Biochem.* **34**, 113 (1987).
5. J. B. Lawrence, R. H. Singer, *Cell* **45**, 407 (1986).
6. M. Segura, U. Lindberg, *J. Biol. Chem.* **259**, 3949 (1984).
7. C. B. Shuster, A. Y. Lin, R. Nayak, I. M. Herman, *Cell Motil. Cytoskeleton* **35**, 175 (1996).
8. Y. T. Kwon *et al.*, *Science* **297**, 96 (2002).
9. A. Varshavsky, *Nat. Cell Biol.* **5**, 373 (2003).
10. K. C. Holmes, D. Popp, W. Gebhard, W. Kabsch, *Nature* **347**, 44 (1990).

10.1126/science.1130813

APPLIED PHYSICS

Tunneling Across a Ferroelectric

Evgeny Y. Tsybmal and Hermann Kohlstedt

Spontaneously polarized materials through which electrons pass by tunneling may be used in novel electronic devices and may reveal new basic physics at the nanometer scale.

The phenomenon of electron tunneling has been known since the advent of quantum mechanics, but it continues to enrich our understanding of many fields of physics, as well as offering a route toward useful devices. A tunnel junction consists of two metal electrodes separated by a nanometer-thick insulating barrier layer, as was first discussed by Frenkel in 1930 (1). Although forbidden by classical physics, an electron is allowed to traverse a potential barrier that exceeds the electron's energy. The electron therefore has a finite probability of being found on the opposite side of the barrier. A famous example is electron tunneling in superconducting tunnel junctions, discovered by Giaever, that allowed measurement of important properties of superconductors (2, 3). In the 1970s, spin-dependent electron tunneling from ferromag-

netic metal electrodes across an amorphous Al_2O_3 film was observed by Tedrow and Meservey (4, 5). The latter discovery led Jullière to propose and demonstrate a magnetic tunnel junction in which the tunneling current depends on the relative magnetization orientation of the two ferromagnetic electrodes (6), the phenomenon nowadays known as tunneling (or junction) magnetoresistance (7). New kinds of tunnel junctions may be very useful for various technological applications. For example, magnetic tunnel junctions have recently attracted considerable interest due to their potential application in spin-electronic devices such as magnetic field sensors and magnetic random access memories.

The range of insulators for tunnel barriers is not limited to Al_2O_3 , however. For example, De Teresa *et al.* studied tunnel junctions with epitaxial perovskite SrTiO_3 barriers to demonstrate the decisive role of interfaces in spin-dependent tunneling (8). Parkin *et al.* (9) and Yuasa *et al.* (10) found large magnetoresistance in crystalline tunnel junctions with MgO barriers. Despite the diversity of materials used in tunnel junctions, the common feature of almost all the existing tunnel junctions is that

E. Y. Tsybmal is in the Department of Physics and Astronomy, Nebraska Center for Materials and Nanoscience, University of Nebraska, Lincoln, NE 68588, USA. E-mail: tsymbal@unl.edu. H. Kohlstedt is at the Institut für Festkörperforschung, Forschungszentrum Jülich, D-52425 Jülich, Germany, and the Department of Materials Science and Engineering, University of California, Berkeley, CA 94720, USA.